RSC Advances

PAPER

View Article Online
View Journal | View Issue

Cite this: *RSC Adv.*, 2020, **10**, 28523

Cobalt doped $BiVO_4$ with rich oxygen vacancies for efficient photoelectrochemical water oxidation†

Guoquan Liu,[a] Fei Li,*[a] Yong Zhu,[a] Jiayuan Li[a] and Licheng Sun[ab]

Received 1st March 2020
Accepted 12th July 2020

DOI: 10.1039/d0ra01961e

rsc.li/rsc-advances

A facile electrodeposition method was developed to prepare Co-$BiVO_4$ thin films with rich oxygen vacancies. The resulting photoanode exhibited a photocurrent density of 3.5 mA cm^{-2} 1.23 V (*vs.* reversible hydrogen electrode (RHE), AM 1.5 G), which is over two times higher than that of undoped $BiVO_4$.

Solar-driven photoelectrochemical (PEC) hydrogen production is a promising method towards clean energy. Among the candidate semiconductors for PEC water oxidation, monoclinic bismuth vanadate ($BiVO_4$) as a promising photoanode material has attracted extensive attention due to its appropriate band gap (2.4–2.6 eV) with a VB edge position of ~2.40 V *vs.* RHE, enabling absorption up to 9.2% of the photon flux in the solar spectrum.[1–7] However, the solar hydrogen conversion efficiency of $BiVO_4$ is still limited by its high charge recombination and poor surface reaction kinetics.[8–12]

Defect engineering has been widely used in electrocatalytic and photocatalytic water oxidation.[13–16] The presence of defects can play an important role in leaking more active sites and increasing the active centers.[17–19] For example, ultrathin spinel structured nanosheets with rich oxygen deficiencies have been evidenced as an excellent catalyst for electrocatalytic water oxidation. The presence of oxygen vacancy was found to increase the synergistic interplay between the number and the reactivity of active sites.[20] Wang and co-workers prepared an efficient Co_3O_4 electrocatalyst with rich oxygen vacancies by plasma-engraving, where the oxygen vacancies on Co_3O_4 surface improve the electronic conductivity and create more active sites for OER.[21] Pan and co-workers utilized multi-step deposition to fabricate multi-layer $BiVO_4$ films with rich oxygen vacancies, which drastically enhances the photocatalytic activity of water oxidation.[22] On the other hand, doping foreign elements is a promising strategy to tune the electrical properties of semiconductor materials.[23–26] During the doping process, heteroatom dopants with different valence and size may play an additional role in introducing and stabilizing the oxygen vacancies.[27,28] For instance, Jiang and Miao synthesized Zn-doped CoOOH with the abundance of oxygen vacancies and demonstrated that the oxygen vacancies were formed when the lower valence-state Zn occupies the lattice site of Co.[29] Ding and co-workers also report that Mo doping on $BiVO_4$ surface may introduce surface oxygen quasi-vacancies based on density functional theory computations. The presence of the oxygen vacancies was suggested to improve the adsorption of water molecules and enhance photocatalytic activity.[30]

Motivated by the above results, we report here the fabrication of the oxygen-vacancy-rich $BiVO_4$ photoanode by means of cobalt doping. In this strategy, the dopant Co^{2+} cations partially occupy the lattice sites of Bi^{3+} in $BiVO_4$ and the $BiVO_4$ crystals tend to maintain the charge balance by forming oxygen vacancies. Theoretical calculations support that the formation energy of oxygen vacancies is significantly reduced in cobalt doped $BiVO_4$ (Co-$BiVO_4$). The resulting oxygen vacancies could potentially act as catalytic active sites to promote OER performance. As a result, the cobalt doped $BiVO_4$ film gave a photocurrent density of 3.5 mA cm^{-2} at 1.23 V *vs.* RHE with a negatively shifted onset potential of 250 mV under AM 1.5 G (100 mW cm^{-2}) solar illumination. The photocurrent reported here is the highest value among the doped $BiVO_4$ electrodes without the assistance of co-catalysts.

As shown in Scheme 1, electrodeposition of a solution containing *p*-benzoquinone, KI and $Bi(NO_3)_3$ gave perpendicularly oriented nanoflakes of BiOI (Fig. 1a).[31] By addition of $CoCl_2$ as a dopant, a potato-chip-like nanoflakes BiOI was obtained (Fig. 1c), the thin nanoflakes with curved wall are interconnected to form a reticulated porous microstructure. Both precursors gave interconnected nano-worms $BiVO_4$ after heating in a muffle furnace at 450 °C (Fig. 1b and d).

The Energy Dispersive X-ray Spectroscopy (EDS) in Fig. 1e confirms the homogeneous distribution of Co elements in Co-$BiVO_4$ nano-worms. Fig. S1† shows the EDS results of 10Co-$BiVO_4$ (abbreviated as Co-$BiVO_4$), indicating the representative $BiVO_4$ photoanode has Co atoms around 1.5 at% of the doping level. The high-resolution electron microscopy (HRTEM) revealed a lattice spacing of 0.26 nm, which is a well agreement with the (200) facets for monoclinic $BiVO_4$ (Fig. 1f).

[a]*State Key Laboratory of Fine Chemicals, DUT-KTH Joint Education and Research Center on Molecular Devices, Dalian University of Technology, Dalian 116024, P. R. China. E-mail: lifei@dlut.edu.cn*

[b]*Department of Chemistry, School of Engineering Sciences in Chemistry, Biotechnology and Health, KTH Royal Institute of Technology, Stockholm 10044, Sweden*

† Electronic supplementary information (ESI) available. See DOI: 10.1039/d0ra01961e

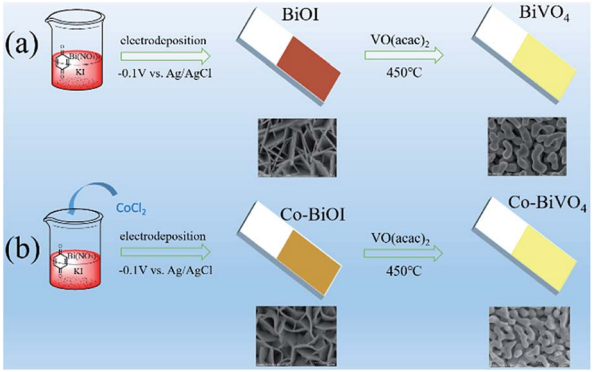

Scheme 1 Schematic description of the fabrication of (a) $BiVO_4$ and (b) Co-$BiVO_4$.

As shown in Fig. 2a, both undoped and doped films showed similar XRD patterns indexed to monoclinic $BiVO_4$, implying that the introduction of Co dopant did not induce phase transformation in $BiVO_4$. In Fig. S2,† the magnified analysis of the XRD pattern shows that the Bragg peak of $BiVO_4$ after Co-doping shifts to a higher value of 2θ, which is in good agreement with the unit lattice shrinkage according to the Bragg equation ($2d \sin\theta = n\lambda$).[28] The shift of characteristic diffraction peaks indicates that Co is incorporated into the $BiVO_4$ matrix and causes $BiVO_4$ lattice distortion, which is consistent with the previous reports.[12] The Raman spectra are also indicative of the monoclinic scheelite crystal structure for $BiVO_4$ and Co-$BiVO_4$ (Fig. 2b), with characteristic signals at 330, 365, 720 and 827 cm^{-1}. The peaks at 330 and 365 cm^{-1} corresponded to the asymmetric and symmetric deformation modes of the VO_4^{3-} tetrahedron ($\delta_{as}(VO^{3-})$ and $\delta_s(VO^{3-})$), respectively.[22] The peak at 827 cm^{-1} was due to the symmetric stretching mode of the V–O bands (ν_s(V–O)). No other diffraction peaks attributed to other phases or impurities were found.

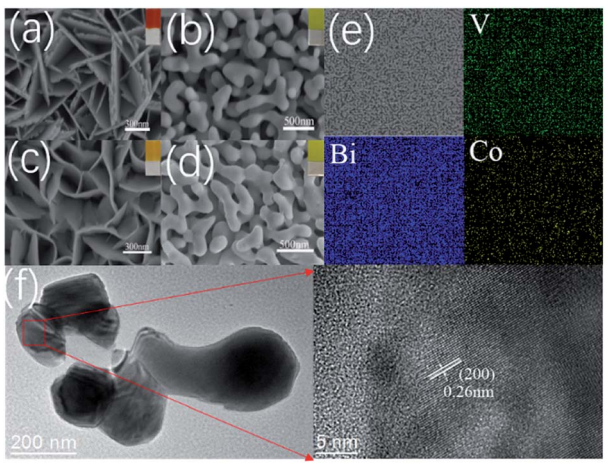

Fig. 1 SEM image (a) BiOI, (b) $BiVO_4$, (c) Co-BiOI, (d) Co-$BiVO_4$, (e) the corresponding elemental mapping images of Co-$BiVO_4$, (f) HRTEM image of Co-$BiVO_4$.

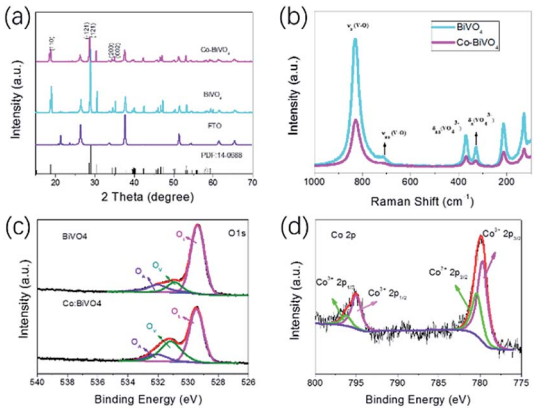

Fig. 2 (a) XRD patterns of $BiVO_4$, Co-BVO_4. (b) Raman spectra of pristine $BiVO_4$ and Co-$BiVO_4$ films. High-resolution XPS spectra of (c) O 1s and (d) Co 2p for the Co-$BiVO_4$ electrode.

To investigate the chemical compositions and their oxidation states, the Co-$BiVO_4$ film was characterized by X-ray photoelectron spectroscopy (XPS). The Bi 4f spectrum is shown in Fig. S1 (ESI†). The peaks located at 159.2 eV (Bi $4f_{7/2}$) and 164.5 eV (Bi $4f_{5/2}$) give evidence to the presence of Bi^{3+}. Based on the V 2p spectrum (Fig. S2, ESI†), two peaks of V 2p at 516.8 eV (V $2p_{3/2}$) and 524.4 eV (V $2p_{1/2}$) were assigned to V^{5+}. The peak at either 780.1 or 795.2 eV in the high-resolution spectrum of Co 2p (Fig. 2d) was deconvoluted into the $2p_{3/2}$ and $2p_{1/2}$ orbitals for Co^{2+} and Co^{3+}, respectively, indicating that Co^{2+} was partially oxidized into cobalt(III) oxide on the surface of Co-$BiVO_4$.[32] The high-resolution O 1s spectra of Co-$BiVO_4$ and $BiVO_4$ samples were fitted into three components at 529.7, 531.3, 532.1 eV (Fig. 2c), corresponding to the O^{2-} species in the lattice (O_L), hydroxyl groups bound to metal cations in the oxygen-deficient region (O_V) and the chemisorbed or dissociated oxygen species from water (O_C).[5] We further explored the effect of different doping concentrations of Co on the oxygen vacancy. As shown in Fig. S5,† the concentration of oxygen vacancy increases with the concentration of doped cobalt. This observation highlights a key role of cobalt in promoting the forming of oxygen vacancies.

The performance of PEC water splitting was measured in 0.5 M borate buffer (pH 9.3) employing a three-electrode configuration with $BiVO_4$ as the working electrode, a platinum wire as the counter electrode and Ag/AgCl as the reference electrode. The PEC water oxidation activities of Co-$BiVO_4$ photoanodes with different Co doping concentrations were shown in Fig. 3a. In general, all Co-doped $BiVO_4$ photoanodes show higher photocurrents than the undoped one. However, photocurrent density of the 12.5Co-$BiVO_4$ electrode is lower than that of 10Co-$BiVO_4$ (abbreviated as Co-$BiVO_4$) electrode. This observation implies that an excess of oxygen vacancies produced by Co doping might become the recombination centers for the electron–hole pairs. When Co-$BiVO_4$ was used as the photoanode, the onset potential for water oxidation was negatively shifted by 250 mV and a notably enhanced photocurrent density of 3.5 mA cm^{-2} at 1.23 V *vs.* RHE was obtained.

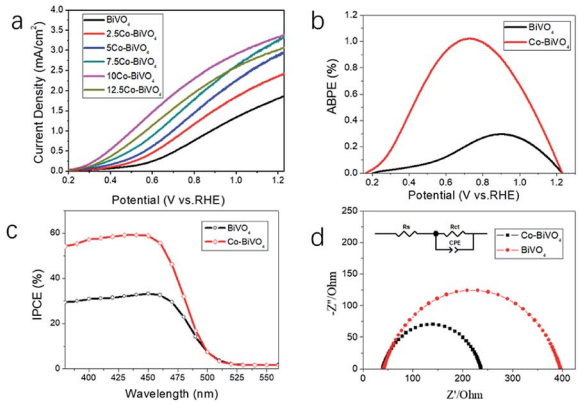

Fig. 3 (a) Photocurrent density *versus* applied potential curves with $BiVO_4$ photoanodes doped with different content of cobalt. (b) ABPE curves of the $BiVO_4$ and Co-$BiVO_4$, (c) IPCE curves at 1.23 V *vs.* RHE, (d) EIS Nyquist plots of $BiVO_4$ and Co-$BiVO_4$ measured at 1.23 V *versus* RHE under AM 1.5 G illumination. The inset shows the equivalent circuit. All the measurements were carried out at 0.5 M sodium borate electrolyte (pH 9.3).

The value acquired here was compared with the data in the literature, which is among the best performance for the doped $BiVO_4$ without co-catalysts reported so far (Table S1, ESI†). Additionally, a photocurrent over 2 mA cm^{-2} at 0.7 V *vs.* RHE was obtained in an extended period of light illumination for 1 h (Fig. S6, ESI†). The slow decrease in the photocurrent is related to the oxidation and consumption of the oxygen vacancies during the PEC reaction.[28] Based on the LSV plots, the maximum applied bias photon-to-current efficiency (ABPE) for the Co-$BiVO_4$ was calculated to be 1.05% at 0.7 V_{RHE} (Fig. 3b), compared to 0.2% for the undoped $BiVO_4$. The incident photon-to-current conversion efficiency (IPCE) as a function of wavelength under 1.23 V_{RHE} was presented in Fig. 3c. Over the visible light range, the IPCE values for Co-$BiVO_4$ reached its maximum of 59% at 460 nm, well matching the corresponding UV-vis absorption spectrum (Fig. S7, ESI†).

Electrochemical impedance spectroscopy (EIS) was conducted at 1.23 V *vs.* RHE under the same conditions used for PEC measurements. According to the Nyquist plots (Fig. 3d), the Co-$BiVO_4$ film featured a smaller resistance than the pristine $BiVO_4$, demonstrating an enhanced conductivity and improved interfacial charge transfer by including cobalt dopants. The surface charge separation efficiency $\eta_{surface}$ was investigated in the presence of 0.5 M sodium sulfite as the hole scavenger. The Co-$BiVO_4$ film exhibited a photocurrent density of 6.10 mA cm^{-2} with a charge separation efficiency of 56% at 1.23 V *vs.* RHE (Fig. S8†). By contrast, the pure $BiVO_4$ electrode showed a poor charge separation of 39% (Fig. S9, ESI†). This result fully agrees with the trend shown by EIS measurements.

The flat band potentials (E_{fb}) and the charge carrier density of pristine $BiVO_4$ and Co-$BiVO_4$ were investigated by Mott–Schottky analysis (MS). Since the charge carrier density was inversely proportional to the slopes of Mott–Schottky plots (Fig. 4a and Table S2, ESI†). The increase of donor density is expected to improve the electrical conductivity and reduce the internal charge transfer resistance.[33] Moreover, the negative shift of E_{fb} from 0.34 to 0.19 V after Co^{2+} doping, which is an advantage for electron accumulation and transport.[28]

To imply the effect of oxygen vacancies on water oxidation, Co-doped $BiVO_4$ photoanode was placed in an electrolyte containing hydrogen peroxide that can efficiently eliminate the oxygen vacancies on electrode. Within a period of 20 minutes, the photocurrent for water oxidation was found to gradually fall from 3.5 to 0.7 mA cm^{-2} at 1.23 V *vs.* RHE (Fig. 4b), providing direct evidence to the correlation between oxygen vacancy and water oxidation activity.[34]

In order to further understand the relationship between Co^{2+} doping and oxygen vacancies, the density functional theory (DFT) calculations were performed (see ESI† for details).[36,37] As shown in the density of states (DOSs) curves in Fig. 4c, the majority of Co 3d orbit stays in the valence band, and there is a small overlap between the Co 3d orbit and the O 2p orbit. Thus, the interaction between Co and the neighbor O atom is weaker than Bi and O atoms at the same sites, making the breaking of Co–O bond much easier.[29] Consequently, more oxygen vacancies were created in Co-$BiVO_4$ over the pure $BiVO_4$. The calculated formation energy of oxygen vacancies for Co-$BiVO_4$ was 1.40 eV, which is smaller than that for the pristine $BiVO_4$ (3.35 eV), supporting our assumption that cobalt doping is an efficient approach for creating oxygen vacancies on $BiVO_4$ (Fig. 4d).

To get insight into the crucial role of the oxygen vacancies of the catalyst in OER,[20,35] the adsorption energy of H_2O molecules was studied by DFT calculations. Fig. S10† indicates that the adsorption energy for a surface with oxygen vacancy is −0.43 eV, which is lower than the oxygen vacancy-free surface with an adsorption energy of −0.28 eV. A possible explanation for the enhancement of absorption energy is that oxygen vacancy would enhance the exposure of surface Bi atoms, which have been suggested to be the active sites for H_2O adsorption.[28,30]

In conclusion, we have successfully fabricated a cobalt-doped $BiVO_4$ with rich oxygen vacancies by a facile

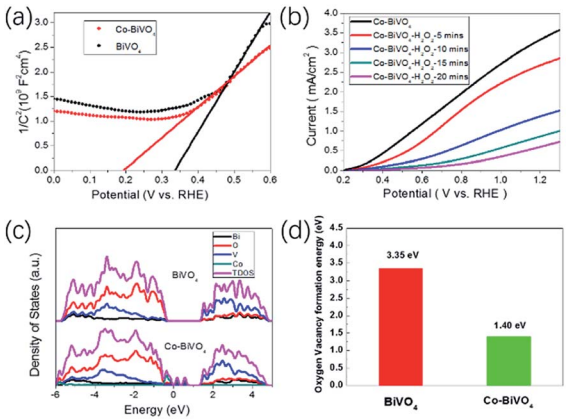

Fig. 4 (a) Mott–Schottky plots collected at a frequency of 1 kHz, (b) *J*–*V* curves of Co-$BiVO_4$ treated with H_2O_2, (c) calculated total and partial density of states of $BiVO_4$ and Co-$BiVO_4$, (d) calculated formation energies of oxygen vacancies for $BiVO_4$ and Co-$BiVO_4$. All measurements were carried out in 0.5 M sodium borate electrolyte (pH 9.3).

electrodeposition method. The DFT calculation evidenced that cobalt-doping facilitates the formation of oxygen vacancies by reducing their formation energy. The resulting Co-$BiVO_4$ photoanode exhibited significantly improved PEC performance than the pure $BiVO_4$ due to reduced H_2O adsorption energy in catalysis and increased carries density that boosting the electrical conductivity of the electrode. Our results are important in demonstrating the correlations between vacancies and foreign element doping in PEC water splitting, which may inspire the further development of photoelectrodes with high efficiency.

Conflicts of interest

There are no conflicts to declare.

Acknowledgements

This work was supported by the National Natural Science Foundation of China (21872016), the Swedish Research Council (2017-00935), the LiaoNing Revitalization Talents Program (XLYC1807125), the Swedish Energy Agency, and K&A Wallenberg Foundation.

References

1 T. W. Kim and K.-S. Choi, *Science*, 2014, **343**, 990–994.
2 Q. Meng, B. Zhang, L. Fan, H. Liu, M. Valvo, K. Edstrom, M. Cuartero, R. De Marco, G. A. Crespo and L. Sun, *Angew. Chem., Int. Ed.*, 2019, **58**, 2–9.
3 H. Ren, T. Dittrich, H. Ma, J. N. Hart, S. Fengler, S. Chen, Y. Li, Y. Wang, F. Cao, M. Schieda, Y. H. Ng, Z. Xie, X. Bo, P. Koshy, L. R. Sheppard, C. Zhao and C. C. Sorrell, *Adv. Mater.*, 2019, **31**, 1807204.
4 M. García-Tecedor, D. Cardenas-Morcoso, R. Fernández-Climent and S. Giménez, *Adv. Mater. Interfaces*, 2019, **6**, 1900299.
5 S. Wang, P. Chen, Y. Bai, J. H. Yun, G. Liu and L. Wang, *Adv. Mater.*, 2018, **30**, 1800486.
6 Y. Peng, G. V. Govindaraju, D. K. Lee, K. S. Choi and T. L. Andrew, *ACS Appl. Mater. Interfaces*, 2017, **9**, 22449–22455.
7 M. Huang, C. Li, L. Zhang, Q. Chen, Z. Zhen, Z. Li and H. Zhu, *Adv. Energy Mater.*, 2018, **8**, 1802198.
8 F. Yu, F. Li, T. Yao, J. Du, Y. Liang, Y. Wang, H. Han and L. Sun, *ACS Catal.*, 2017, **7**, 1868–1874.
9 B. B. Zhang, X. J. Huang, H. Y. Hu, L. J. Chou and Y. P. Bi, *J. Mater. Chem. A*, 2019, **7**, 4415–4419.
10 S. Wang, T. He, J.-H. Yun, Y. Hu, M. Xiao, A. Du and L. Wang, *Adv. Funct. Mater.*, 2018, **28**, 1802685.
11 S. Wang, P. Chen, J. H. Yun, Y. Hu and L. Wang, *Angew. Chem., Int. Ed.*, 2017, **56**, 8500–8504.
12 B. Zhang, H. Zhang, Z. Wang, X. Zhang, X. Qin, Y. Dai, Y. Liu, P. Wang, Y. Li and B. Huang, *Appl. Catal., B*, 2017, **211**, 258–265.
13 H. Tan, Z. Zhao, W. B. Zhu, E. N. Coker, B. Li, M. Zheng, W. Yu, H. Fan and Z. Sun, *ACS Appl. Mater. Interfaces*, 2014, **6**, 19184–19190.
14 Y. Liu, C. Ma, Q. Zhang, W. Wang, P. Pan, L. Gu, D. Xu, J. Bao and Z. Dai, *Adv. Mater.*, 2019, **31**, 1900062.
15 R. Liu, Y. Wang, D. Liu, Y. Zou and S. Wang, *Adv. Mater.*, 2017, **29**, 1701546.
16 Y. Zhao, Y. Zhao, R. Shi, B. Wang, G. I. N. Waterhouse, L. Z. Wu, C. H. Tung and T. Zhang, *Adv. Mater.*, 2019, **31**, 1806482.
17 L. Zhuang, L. Ge, Y. Yang, M. Li, Y. Jia, X. Yao and Z. Zhu, *Adv. Mater.*, 2017, **29**, 1606793.
18 W. J. Xu, F. L. Lyu, Y. C. Bai, A. Q. Gao, J. Feng, Z. X. Cai and Y. D. Yin, *Nano Energy*, 2018, **43**, 110–116.
19 K. Zhang, G. Zhang, J. Qu and H. Liu, *Small*, 2018, **14**, 1802760.
20 J. Bao, X. Zhang, B. Fan, J. Zhang, M. Zhou, W. Yang, X. Hu, H. Wang, B. Pan and Y. Xie, *Angew. Chem., Int. Ed.*, 2015, **54**, 7399–7404.
21 L. Xu, Q. Jiang, Z. Xiao, X. Li, J. Huo, S. Wang and L. Dai, *Angew. Chem., Int. Ed.*, 2016, **55**, 5277–5281.
22 J.-M. Wu, Y. Chen, L. Pan, P. Wang, Y. Cui, D. Kong, L. Wang, X. Zhang and J.-J. Zou, *Appl. Catal., B*, 2018, **221**, 187–195.
23 H. Miaoyan, B. Juncao, X. Wei, H. Chao and Z. Ruiqin, *J. Mater. Chem. A*, 2018, **6**, 3602–3609.
24 M. N. Shaddad, P. Arunachalam, J. Labis, M. Hezam and A. M. Al-Mayouf, *Appl. Catal., B*, 2019, **244**, 863–870.
25 S. Qin, M.-L. Sebastián, T. Pengyi, F. Cristina, R. M. Joan, B. Zhaoyong, W. Hui and A. Teresa, *ACS Catal.*, 2018, **8**, 3331–3342.
26 L. Han, S. Dong and E. Wang, *Adv. Mater.*, 2016, **28**, 9266–9291.
27 X. Yang, A. J. Fernandez-Carrion, J. Wang, F. Porcher, F. Fayon, M. Allix and X. Kuang, *Nat. Commun.*, 2018, **9**, 4484.
28 Q. G. Pan, K. R. Yang, G. L. Wang, D. D. Li, J. Sun, B. Yang, Z. Q. Zou, W. B. Hu, K. Wen and H. Yang, *Chem. Eng. J.*, 2019, **372**, 399–407.
29 J. S. Wang, J. Liu, B. Zhang, F. Cheng, Y. J. Ruan, X. Ji, K. Xu, C. Chen, L. Miao and J. J. Jiang, *Nano Energy*, 2018, **53**, 144–151.
30 K. Ding, B. Chen, Z. Fang, Y. Zhang and Z. Chen, *Phys. Chem. Chem. Phys.*, 2014, **16**, 13465–13476.
31 Y. Wang, F. Li, X. Zhou, F. Yu, J. Du, L. Bai and L. Sun, *Angew. Chem., Int. Ed.*, 2017, **56**, 6911–6915.
32 F. Wang, Z. B. Liu, K. X. Wang, X. D. Zhu, X. H. Fan, J. Gao, Y. J. Feng, K. N. Sun and Y. T. Liu, *Chem. Commun.*, 2018, **54**, 5138–5141.
33 Q. Shi, X. Song, H. Wang and Z. Bian, *J. Electrochem. Soc.*, 2018, **165**, H3018–H3027.
34 B. Zhang, L. Wang, Y. Zhang, Y. Ding and Y. Bi, *Angew. Chem., Int. Ed.*, 2018, **57**, 2248–2252.
35 G. Wu, N. Li, D. R. Zhou, K. Mitsuo and B. Q. Xu, *J. Electrochem. Soc.*, 2004, **177**, 3682–3692.
36 G. Kresse and J. Hafner, *Phys. Rev. B: Condens. Matter Mater. Phys.*, 1993, **47**, 558–561.
37 G. Kresse, *Phys. Rev. B: Condens. Matter Mater. Phys.*, 1996, **54**, 11169–11186.

